Plasma–photocatalyst coupling for Ethanol removal using porous manganese oxide-TiO_2

Imen Aouadi[a], Semy Ben Chaabene[b], Jean-Michel Tatibouët[b], Latifa Bergaoui[a,c,*]

[a] *Laboratoire de Chimie des Matériaux et Catalyse, Faculté des Sciences de Tunis, Université Tunis El Manar, Tunis, Tunisia.*
[b] *Institut de Chimie des Milieux et Matériaux de Poitiers, UMR CNRS 7285, Université de Poitiers, Ecole Nationale Supérieure d'Ingénieurs de Poitiers (France).*
[c] *Institut National des Sciences Appliquées et de Technologie, Université de Carthage, Tunis, Tunisia.*

(Received: 27 March 2017, accepted: 19 June 2017)

Abstract: β-MnO_2-TiO_2, birnessite-TiO_2 and todorokite-TiO_2 systems were prepared in the aim to be used as catalysts in the removal of Ethanol from air. First, prepared solids were characterized by X-ray diffraction, N_2-physisorption, Raman spectroscopy, Scanning Electron Microscopy, H_2-Temperature-programmed reduction and photoluminescence. Second, they were tested in the Ethanol oxidation reaction (at low concentration) under ultraviolet light and under non-thermal plasma. The combination of those both technologies was also tested. A comparative study of different catalysts shows that the Mn oxidation state, the structure of Mn oxides, VOCs adsorption capacity and mobility of oxygen could play a key role in the Ethanol oxidation and in the minimization of the undesirable by-products. Besides, the combination of photocatalysis with NTP increased significantly the conversion of Ethanol and decreased the ozone residual concentration.

Keywords: Non-thermal plasma, Photocatalysis, Birnessite, Todorokite, VOCs.

INTRODUCTION

Because of the volatile organic compounds (VOCs) harmfulness for humans -especially in closed environment [1]- several methods have been tested to limit their presence in air (adsorption, membrane separation, bioreaction...). However, these methods are not always efficient when low concentration of VOCs needs to be treated [2,3]. In the last decade, the photocatalysis and the non thermal plasma (NTP) technologies were widely studied for COVs oxidation due to their high efficiency and quick response at ambient temperature [4,5], but each of these technologies has some limitations. NTP generates some toxic by-products (such as ozone) with low carbon dioxide selectivity. If the photocatalysis is an interesting way for organic molecules elimination in aqueous solution, its efficiency in oxidation of air pollutants is rather limited [6,7]. To overcome such problems, recent researches were focused on the coupling of NTP and UV photocatalysis. Moreover, recent publications have shown that a possible synergy effect could be observed when a catalyst was simultaneously submitted to non thermal plasma and UV irradiation [8-11]. Recently, [12] we have shown the efficiency of Mn_3O_4-TiO_2 systems in the Ethanol decomposition over UV, NTP and especially when NTP is coupled with UV photocatalysis. We have proposed that, on Mn_3O_4 ($Mn^{II}Mn^{III}{}_2O_4$) the O_3 activation can be carried out by a redox mechanism leading to the oxidation of Mn(II) and Mn(III) to Mn(III) and Mn(IV) respectively.

The aim of the current study is to test, in the same conditions, the efficiency of Mn(III)/Mn(IV) manganese oxides. Mn mixed-valent layer and tunnel structure manganese dioxides usually referred to as phyllomanganates and tectomanganates respectively, were used and compared to b-MnO_2 after mixing with TiO_2. The efficiency of the Ethanol decomposition under UV alone, NTP alone and the combined process UV/NTP was

* Corresponding author, e-mail address : latifa.bergaoui@insat.rnu.tn

investigated experimentally at atmospheric conditions. Surface dielectric barrier discharge (DBD) was used for the generation of plasma process.

EXPERIMENTAL SECTION

1. Catalysts Preparation

1.1. Reactants

Manganese nitrate hexahydrate: $Mn(NO_3)_2$, $6H_2O$, manganese oxide: (β-MnO_2), potassium permanganate: $KMnO_4$, sodium hydroxide: NaOH and commercial TiO_2 powder (P25) were purchased from Sigma Aldrich.

1.2. Birnessite synthesis

A 33.5 mL of an aqueous solution of manganese (II) nitrate (0.50 mol L^{-1}) was stirred vigorously with 70 mL of an aqueous solution of NaOH (4.0 mol L^{-1}) at room temperature. After stirring for 15 min, 50 mL of an aqueous potassium permanganate solution (0.1 mol L^{-1}) was added. Stirring was maintained for 7 days; the resulting suspension was isolated by centrifugation and then dried at 333 K. This sample was named **bir** for birnessite.

1.3. Todorokite synthesis

0.5 g of the already prepared birnessite was dispersed under magnetic stirring in 35 mL of $MgCl_2$ aqueous solution (1.5 mol L^{-1}) for 24 h at room temperature. The suspension obtained was washed 3 times with distilled water and then centrifuged. This solid suspension was then transferred into a Teflon vessel containing 15 mL of distilled water. The Teflon vessel was then placed in a stainless steel autoclave and put in the oven at 180°C for 2 days (hydrothermal treatment). Finally, the obtained suspension was centrifuged at 8500 rpm and then dried at 333 K for 24 h. This sample was named **tod** for todorokite.

1.4. Preparation of Mn oxide-TiO_2 Catalysts

Approximately 20 mg of each manganese oxide (birnessite, todorokite or commercial β-MnO_2) was added to a dispersion of 2 g of TiO_2-P25 in 20 mL of ultra-pure water and kept under stirring during 10 min. This mixture was then treated for 10 min in an ultrasonic bath and finally dried at 200°C for 4 h.

1.5. Fiber Glass Supported Catalysts Preparations

The glass fibers fabrics were used as a mechanical support for catalytic active phase. The samples (100 × 170 mm) were immersed in a hydrochloric acid solution (4 mol L^{-1}) for 3 h and then washed three times with 750 mL of distilled water and then dried at 120°C for 4 h. 0.5 g of each catalyst (TiO_2 or MnO_x-TiO_2) was added to 10 mL of water and treated during 10 min in an ultrasonic bath. The obtained liquid paste was then deposited on the glass fibers and dried at 110°C overnight. The catalyst concentration on the glass fiber is estimated to around 30 g m^{-2}.

2. Characterization Techniques

The X-ray powder diffraction (XRD) patterns of all samples were recorded on an X'Pert Pro Panalytical diffractometer using CuKα radiation (k = 1.54186 Å). Specific surface area and pore volume measurements of the samples were done by N_2 adsorption at 77 K using a Micromeritics ASAP 2020 apparatus. The samples were outgassed in vacuum during 6 h at 200°C prior to the nitrogen adsorption. For the temperature-programmed reduction (TPR) a system equipped with a TCD detector was used. In the experiments, 50 mg of sample were placed in a U-shape tube reactor and reduced by a gas mixture 10% H_2/Ar, at a flow rate of 50 mL min^{-1}. A heating rate of 10°C min^{-1} from room temperature to 800°C was used. The samples were also examined using a JEOL 3400 Field Emission Scanning Electron Microscopy with Energy Dispersive System (FE-SEM-EDX). Raman spectroscopy was performed using a HORIBA JOBIN–YVON LabRAM HR800UV confocal micro spectrometer (514.5 nm laser excitation wavelength and 0.05 mW power at the sample) calibrated with a silicon sample. Photoluminescence (PL) spectroscopy of synthesized products was taken at room temperature on a Perkin Elmer Lambda S55 (LS55) spectrofluorometer using a Xe lamp with an excitation wavelength of 364 nm.

3. Experimental Setup and Analyses Procedure

The experimental setup of VOCs degradation by non-thermal plasma and photocatalysis includes a VOCs generator, a specific cylindrical DBD plasma reactor and an exhaust gas analysis section. The specific energy was fixed at E_{spe} = 14 J L^{-1} (P = 0.95 W) for all experiments. This rather low value of specific energy avoids a noticeable formation of NOx which remains in the ppb range. Ethanol was evaporated by a Bronkhorst system and mixed with air before being introduced into the reactor. The flow rate and Ethanol concentration were adjusted by mass flow controllers. Ethanol concentration was fixed to 30 ppm at a total flow rate (air-Ethanol) of

4 L min^{-1}. The space velocity through the plasma/ photocatalytic zone was 1640 h^{-1} (residence time 2.9 s), calculated at ambient temperature and pressure. A specific DBD plasma-catalyst reactor allowing submitting simultaneously the catalyst to plasma and UV irradiation was built [13]. This reactor allows using NTP alone, UV photocalysis alone (Philips UV lamp: TL 8 W/10 FAM; maximum light intensity output at 364 nm) and NTP and UV photocatalysis coupled. A Varian 430 -GC gas and a Varian CP-4900 Micro GC chromatographs were used to analyze on-line (before and after the reactor) the Ethanol and the reaction products. Ozone was analyzed by an ozone analyzer (Dual Beam 205 InDevR 2B).

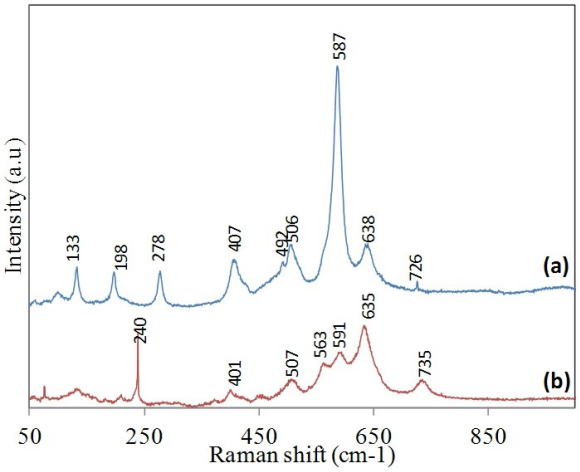

Fig 2. Raman spectra of (a) bir and (b) tod.

RESULTS AND DISCUSSION

1. Manganese oxides characterization

The X-ray diffractions patterns of both commercial and elaborated manganese oxides are shown on figure 1. The XRD pattern of the commercial manganese oxide (Fig. 1-a) gives peaks identical to the pure phase of β-MnO_2 (pyrolusite) according to the reported data (JCPDS 24- 0735) with tetragonal symmetry space group. For this oxide the oxidation state of manganese is (IV) with a [1×1] tunnel structure which corresponds to a single octahedral chains connected by corner-sharing. The diffraction pattern of bir sample (Fig. 1-c) can be indexed to the monoclinic phase of birnessite, which is compatible with the standard value of JCPDS file 043-1456, already described in the literature [14]. The birnessite oxide is characterized by an octahedral layered structure. The interlayer distance is estimated to 0.71 nm from the diffraction lines at 2θ = 12° [15]. After ion-exchange and hydrothermal reactions, the birnessite oxide was transformed into the todorokite phase. Indeed, the XRD pattern at figure 1-b reveals the presence of two reflections at 2θ = 9.3° and 19°. These reflections can be perfectly indexed to the monoclinic todorokite phase according to the standard data file JCPDS 013-0164. Todorokite is a tunnel type of manganese dioxide with 1D [3x3] octahedral tunnels structure through the b-axis [16,17]. The inter-reticular distance of the (100) plane, of the prepared todorokite is 0.93 nm, which reflects the larger size of the tunnel present in this oxide [15-17]. The average crystallite size values, calculated from XRD patterns by applying the Debye Scherer formula have been found to be about 6.0, 2.3 and 1.5 µm, for β-MnO_2, tod and bir samples, respectively. Figure 2 shows the Raman spectra of the as-synthesized manganese oxides. Figure 2-a shows a similar spectrum to those reported previously for several manganese oxides with birnessite-type structures [18,19]. The Raman band located at about 638 cm^{-1} is viewed as the symmetric Mn-O stretching vibration of MnO_6 groups. Also, a strong Raman band centered at 587 cm^{-1} is attributed to the ν_3 (Mn-O) stretching vibration of basal MnO_6 sheets [18,20]. The three bands located at 506, 492 and 407 cm^{-1} are related to Mn-O-Mn in the MnO_2 octahedral lattice. Finally, the band at 278 cm^{-1} is attributed to vibration modes of hydrated cations interlayer ($Na(H_2O)_n^+$) [19]. The observed Raman spectrum

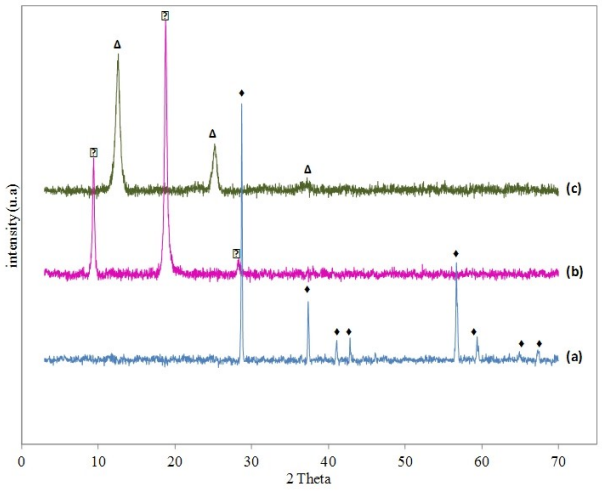

Fig 1. XRD patterns of (a) commercial β-MnO_2, (b) tod and (c) bir. ♦ β-MnO_2, ? tod, Δ bir.

of todorokite (Fig. 2-b) has several bands as already described by Kim et al. [21]. For this author, a large band centered at 620 cm^{-1} is characteristic of todorokite (symmetric Mn-O stretching of the MnO_6 octahedral) with a width at half-height greater than 70 cm^{-1} which likely corresponds to the superposition of several bands [22]. Then, the three bands observed at figure 2-b at 635, 591 and 563 cm^{-1} may correspond to a better resolution of the band at 620 cm^{-1}. Also the band at 240 cm^{-1} was attributed to todorokite. However, the other bands observed in this spectrum are probably originated from impurities (birnessite and/or β-MnO_2). The abundance of these minority phases is not proportional to the relative intensities of observed bands. Indeed, as reported by Julien and Massot [18] for the oxides of manganese whose structure results from the combination of octahedron MnO_6, the Raman bands intensities are inversely proportional to the number of shared edges per MnO_6 octahedron. For todorokite, the average number of shared edges is very important which could explain the low band intensity of todorokite as compared to impurities ones. Raman spectroscopy seems to be a very interesting tool to detect any impurities accompanying todorokite.

Figure 3 show the SEM image of bir and tod samples. The birnessite sample (fig. 3-a) shows a flower-like plate morphology, whereas Todorokite (Fig. 3-b) shows both platelet and needle shaped crystallites [23]. In order to study the effect of the oxidation states of manganese on the reactivity of the synthesized catalysts, the TPR-H_2 analysis was carried out for our manganese oxides (b-MnO_2, bir and Tod). TPR profiles are presented in figure 4. The commercial β-MnO_2 (Fig. 4-a) shows three reduction peaks located at 375, 500 (shoulder) and 585°C which can be described by the successive reduction processes: $MnO_2 \rightarrow Mn_2O_3 \rightarrow Mn_3O_4 \rightarrow MnO$ [24,25]. The TPR profile of birnessite (Fig 4-c) shows the same reduction process but at lower

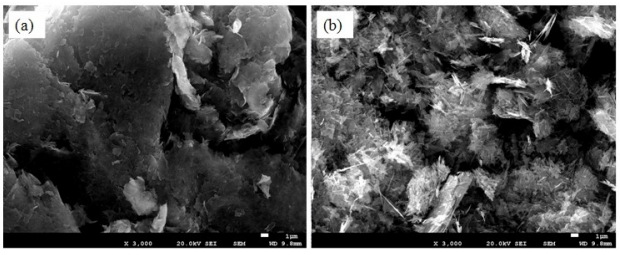

Fig 3. SEM micrograph of (a) bir and (b) tod.

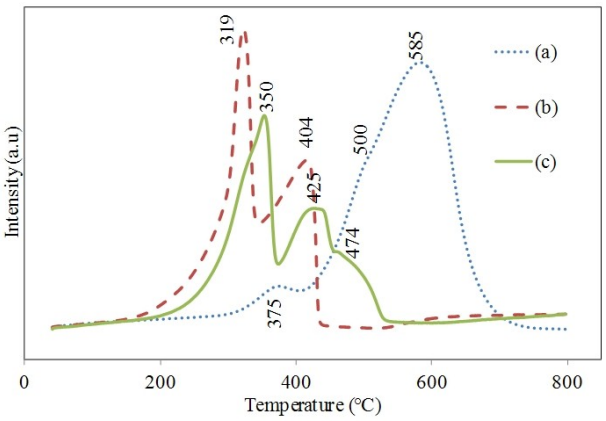

Fig 4. H_2-TPR profile of (a) β-MnO_2, (b) tod and (c) bir.

temperatures. Indeed, the three bands of reductions are located at 350, 425 and 474°C. However, the TPR profile of todorokite (Fig. 4-b) shows only two reduction peaks at 319 and 404°C, which corresponds to the following reduction process: Mn(IV) → Mn(III) → Mn(II). However, the lower the temperature the higher the reducibility is. The TPR-H_2 profiles could then reflect the oxygen mobility in the samples. Indeed, the most reducible one has more mobile oxygen at the surface and by volume [26,27] which can be beneficial in catalysis and photocatalysis activity. Then, studied manganese oxides follow the reducible order: Tod > bir > β-MnO_2. X-ray diffractograms of the Mn oxide-TiO_2 systems are presented on figure 5. All diffraction patterns show reflection assigned to anatase and rutile phases. The manganese oxide phase was only detectable for β-MnO_2-P25 and

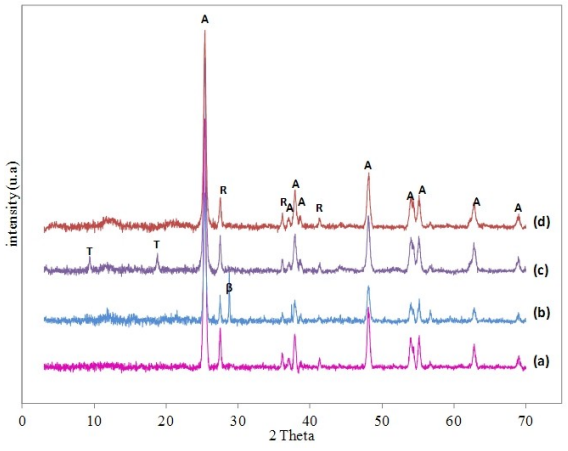

Fig 5. XRD patterns of (a) TiO_2, (b) β-MnO_2-TiO_2, (c) Tod-TiO_2, (d) Bir-TiO_2. (A) anatase, (R) rutile, (T) tod et (β) β-MnO_2

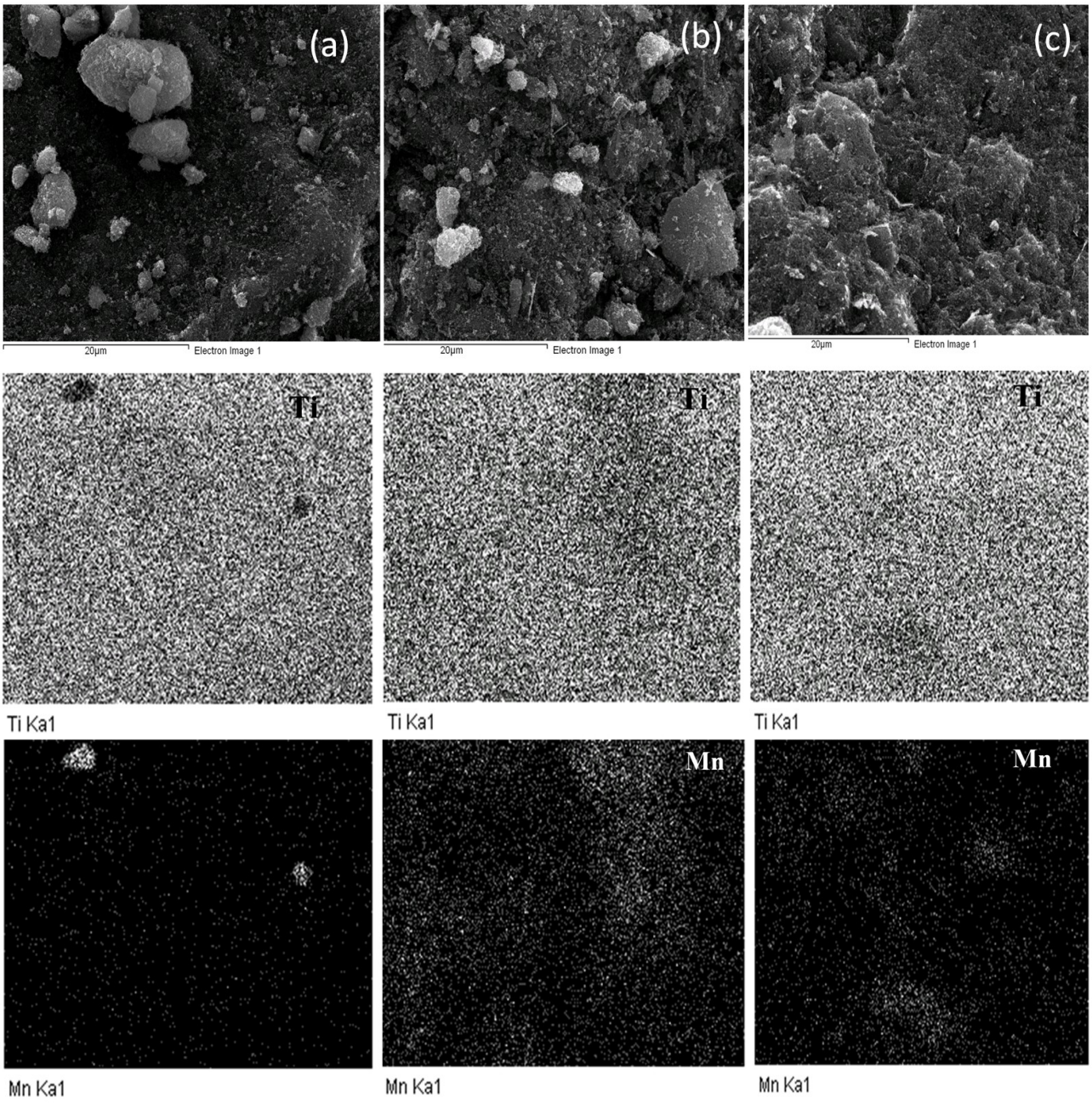

Fig 6. SEM micrograph and Ti and Mn elemental mapping of (a) β-MnO_2, (b) tod and (c) bir samples.

Tod-P25 samples which show reflection corresponding to β-MnO_2 and todorokite respectively. This could be attributed to their high degree of crystallinity compared to the lamellar oxide. Figure 6 shows SEM micrographs and elemental mapping. Mn elemental mapping images show the distribution of manganese on the Mn oxide-TiO_2 samples. The best Mn dispersion is observed for bir-TiO_2 (Fig. 6-c) sample while the most heterogeneous is observed for β-MnO_2-TiO_2 sample (Mn seems form some white spots, which suggested that Mn was not well distributed) (Fig.6-a) [28]. These observations are consistent with the highest particle size of β-MnO_2 and the lowest one for birnessite.

The PL phenomena of excited energy higher or equal to the band gap energy of semiconductor are related to transfer behavior of the excited electrons and the photo-induced holes, either in the generation process of this hole or in the

recombination phenomenon of photo-induced charge carriers [29]. Figure 7 shows the PL spectra of the commercial TiO_2-P25 and prepared samples b-MnO_2-P25, Tod-P25 and bir-P25 under the excitation wavelength of the 315 nm. In this work, we used this excitation wavelength because it corresponds to the maximum light intensity power of the UV source used for the photocatalytic test. As seen from PL spectrum of TiO_2-P25, two intense emission peaks can be identified at around 420 and 484 nm and some weak and broad emissions between 500 and 600 nm. The first emission peak can be attributed to the emission due to the recombination of self-trapped or free excitons [30,31]. The second TiO_2 emissions have been reported to be due to oxygen vacancies and to the oxygen related to defect centers [32]. It is found that the addition of MnO_x causes a significant increase in the intensity of these two peaks, suggesting a quickening recombination rate of photo-generated electrons and holes. Moreover, we noted that this increase follows the order: β-MnO_2-P25 < bir-P25 < tod-P25. This behavior can be explained by the oxidation states and reducibility of these oxides and this confirms the results obtained by temperature programmed reduction analysis. In fact, the reducibility order of these oxides obtained by TPR analysis, is as follows: β-MnO_2 < bir < tod. Indeed, the better reducibility in the case of todorokite might derive from the presence of more surface oxygen vacancies, thus greatly enhancing the mobility of oxygen species [33], which favors the presence of some different hydroxyl groups (Mn-OH). Therefore, the modification of the surface state of the catalyst increases the possibility of electron/ hole (e^-/h^+) recombination and increases the intensity of the PL spectrum. So, the highest reducibility and the coexistence of two oxidation states increase the recombination rate which would inhibit the photocatalytic reaction.

2. Catalytic Activity

Prepared samples were tested for Ethanol decomposition reaction under different experimental conditions. For the first experiment, only the UV lamp light was turned on. The second experiment was achieved with only the non-thermal plasma. For the third experiment, both UV and NTP are used at the same time. All experiments were performed with the reactor containing glass-fibers (GF) alone or Mn oxide-TiO_2 deposited on glass fibers. Table I shows the results obtained in the conversion of Ethanol, carbon oxides total formation (COx yield) and the CO, CO_2 and Acetaldehyde selectivities. Carbon balance was calculated for each experiment. It was assumed that carbon balance values lower than 100% are due either to adsorption of products on the reactor wall or formation of one or more by-products (like Acetic acid) which are undetected by our analytic system.

2.1. UV Alone Experiment

The photocatalytic decomposition efficiency of Ethanol over GF and MnO_x-TiO_2/GF was evaluated under UV light activation and the results are shown in Table I. When the glass fibers alone were used, low Ethanol conversion is observed (~ 15%) without any detection of CO_2 or Acetaldehyde in the reactor outlet suggesting that a fraction of Ethanol is probably converted to intermediates products (undetectable by our analysis system or adsorbed on the lines and/or the reactor wall). With deposited β-MnO_2-TiO_2 on the glass fibers, Ethanol conversion reaches 53%. The CO_2 selectivity is 76% and the carbon balance is equal to 97%. However, the presence of birnessite and todorokite instead of β-MnO_2 does not enhance the photocatalytic performance, these samples achieved poorer results: lower Ethanol conversion, lower CO_2 selectivity, greater formation of Acetaldehyde and lower carbon balance. These results are consistent with the PL

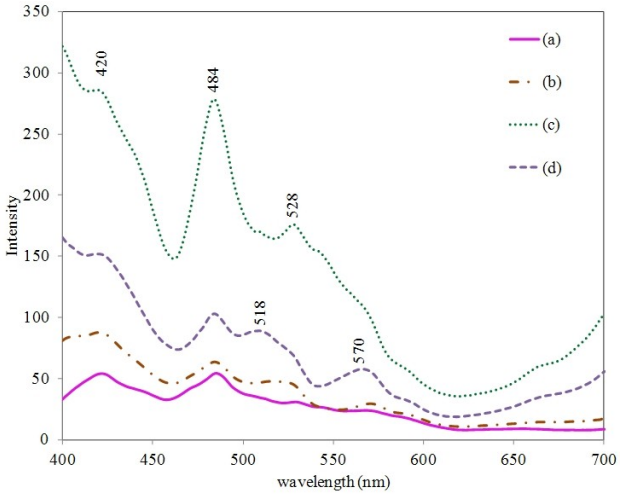

Fig.7 Photoluminescence (PL) spectra of (a) TiO_2, (b) β-MnO_2-TiO_2, (c) tod-TiO_2 and (d) bir-TiO_2 catalysts; λ_{Ex}: 364 nm

Table I: Ethanol conversions, COx yield and CO_2, CO and Acetaldehyde selectivities in photocatalysis, under NTP and under coupling photocatalysis and NTP (Initial Ethanol concentration = 30 ppm, E_{spe} = 14 J.L-1).

Experiments and Catalyst	Conversion EtOH (%)		CO_x yield (ppm)	Selectivity (%)			Carbon balance (%)	Ozone (ppm)
				CO_2	CO	ACA		
UV								
GF	15			0	0	0	-	0
MnO_2-P25/GF	53		25.8	76	0	21	97	0
Bir-P25/GF	29		1.8	10	0	38	48	0
Tod-P25/GF	34		0.6	3	0	31	34	0
NTP								
GF	83		17	23	11	12	46	231
MnO_2-P25/GF	69		19.4	32	15	19	65	112
Bir-P25/GF	72		18.6	31	12	23	66	128
Tod-P25/GF	78		22.0	33	14	21	68	127
UV/NTP								
GF	81	86[a]	18.4	29	9	11	49	63
MnO_2-P25/GF	78	85 [a]	17.4	24	13	15	53	93
Bir-P25/GF	86	80 [a]	31	48	22	11	81	96
Tod-P25/GF	91	85 [a]	44.8	54	28	6	88	87

study conclusions; remember that β-MnO_2-TiO_2 sample shows the lowest PL intensity spectrum compared to those of bir-TiO_2 and tod-TiO_2.

Moreover, the poor dispersion of β-MnO_2 (as shown by SEM micrographs and elemental mapping) could also play a possible role. Indeed, for bir-TiO_2 and tod-TiO_2 samples, the manganese oxide is better dispersed than in β-MnO_2-TiO_2 and could partly cover the photocatalytic TiO_2 surface, reducing then the performances of these catalysts since manganese oxide is inactive in photocatalysis [34,35]. However, even with the best catalyst (β-MnO_2-TiO_2/GF), the obtained experimental results, show that photocatalysis is not enough interesting for the efficient removal of Ethanol at low concentrations.

2.2. NTP Alone Experiment

The catalytic test results, under NTP alone, are presented on Table I. In the presence of glass fibers alone in the reactor, a significant conversion of Ethanol is observed with however a low CO_2 selectivity, a low carbon balance and a high ozone concentration (231 ppm) in the reactor outlet. When Mn oxide-TiO_2 was present, a slight increase in the selectivity of CO_2 and in the carbon balance was observed with a significant decrease in the ozone concentration (compared to GF alone). The presence of a catalyst seems to promote the CO_2 formation, to decrease the undetected products formation, and limits the ozone production. Ethanol conversion and carbon oxides yield increase in the order β-MnO_2-TiO_2 < bir-TiO_2 < tod-TiO_2 following the H_2-TPR reducibility ranking of these samples. The highest activity may be attributed to the chemical structure of Todorokite. Obviously, the dimensions of the channels (3×3) in the tod sample are larger than those of bir and β-MnO_2. Todorokite has also more -OH groups in the channel and higher VOCs adsorption capacity. As reported by several authors [27,36], the tunnel structures with lower accumulated densities of MnO_6 octahedra can be reduced at lower temperature. This higher oxygen mobility in todorokite might explain the good activity of tod-TiO_2 sample compared to the two other

Mn oxides-TiO_2 sample. However, even with the best catalyst a low CO_2 selectivity (33%) is obtained with a poor carbon balance (68%). This may be ascribed to the formation of intermediary products when plasma worked under a low specific energy [36]. However, the benefit of adding manganese oxide concerns the reduction of the residual ozone concentrations. As described by our previous work [12], ozone can react with the catalyst surface to form adsorbed atomic oxygen species and molecular oxygen and could take part in the heterogeneous oxidation reactions [12, 27, 38].

2.3. NTP and UV Coupled Experiment

The results, when NTP and UV are used simultaneously, are presented on Table I. When glass fibers alone are exposed to both NTP and UV, Ethanol conversion and products selectivities are similar to those obtained under NTP alone showing that the addition of UV to NTP does not affect the system GF-NTP since glass fibers has not any photocatalytic properties. However, the presence of UV seems to inhibit the ozone formation observed under NTP without UV or to favor its elimination. The results obtained by using bir-TiO_2 and tod-TiO_2 catalysts show that the UV/NTP coupling allows increasing the Ethanol conversion compared to UV alone and to NTP alone. We should notice that the carbon oxides yield shows a large increase with bir-P25 and Tod-P25, following the H_2-TPR reducibility ranking: β-MnO_2-TiO_2 < bir-TiO_2 < tod-TiO_2. This proved again that the higher mobility of oxygen in todorokite and the better VOCs adsorption capacity plays a positive role in VOCs oxidation under coupled NTP and UV-photocatalysis. A rough calculation by supposing that the conversion of Ethanol due to photocatalysis and to NTP is only additive shows that bir-P25/GF and tod-P25/GF samples have a little synergy effect (the experimental values was 6% higher than the sum of the conversions of UV alone and NTP alone). The decrease of ozone from 231 ppm under NTP alone to 63 ppm under UV associate to NTP (case of glass fiber placed in reactor without any catalysts), suggests that UV could favor ozone decomposition but does not contradict other hypothesis. In fact, the decomposition of ozone in presence of catalyst and under UV irradiation can be explained by two different ways: *i)* ozone acts as electron acceptor and/or *ii)* ozone is decomposed by adsorption of photons [13,39].

CONCLUSION

Three Mn oxides-TiO_2 catalysts were elaborated and evaluated under UV alone, NTP alone and coupled process UV/NTP to decompose Ethanol. The comparative study of different used catalysts shows that under photocatalysis alone, the best catalyst was β-MnO_2-TiO_2/GF, which is supported by PL study results. However, under NTP alone and under coupled process UV/NTP, the best catalyst was tod-TiO_2/GF, which is due to the existence of OH groups, higher VOCs adsorption capacity and higher mobility of oxygen in the sample, according to H_2-TPR results. A slight synergy effect was observed by using bir-TiO_2 and tod-TiO_2 samples under coupled UV/NTP process. This synergy effect has been assigned to the possible activation of the ozone produced by plasma, by the UV radiation in presence of a catalyst.

Acknowledgments: We acknowledge the Tunisian Ministry of High Education, Scientific Research and Technology for the Ph.D. mobility grant of Imen Aouadi and Dr. Mehrez Hermassi for SEM images achieving.

REFERENCES

[1] M. Kampa and E. Castanas, *Environ. Pollut.*, **2008**, 151, 362.
[2] A. M. Vandenbroucke, R. Morent, N. De Geyter, and C. Leys, *J. Hazard. Mater.*, **2011**, 195, 30.
[3] X. Huang, J. Yuan, J. Shi, and W. Shangguan, Journal of Hazardous Materials, **2009**, 171, 827.
[4] H. Huang, D. Ye, and X. Guan, Catalysis Today, **2008**, 139, 43.
[5] A. M. Harling, D. J. Glover, J. C. Whitehead, and K. Zhang, *Appl. Catal. B Environ.*, **2009**, 90, 157.
[6] K. Nakata and A. Fujishima, *J. Photochem. Photobiol. C Photochem. Rev.*, **2012**, 13, 169.
[7] A. Fujishima, X. Zhang, and D. A. Tryk, *Surf. Sci. Rep.*, **2008**, 63, 515.
[8] T. Zhu, J. Li, Y. Jin, Y. Liang, and G. Ma, *Int. J. Environ. Sci. Technol.*, **2008**, 5, 375.
[9] A. Maciuca, C. Batiot-Dupeyrat, and J.-M. Tatibouet, *Proc. 3 Int. CEMEPE SECOTOX Conf.*, **2011,** p. 533.
[10] J. Taranto, D. Frochot, and P. Pichat, *Ind. Eng. Chem. Res*, **2007**, 46, 7611.
[11] R-B. Sun, Z-G. Xi, Fu-H. Chao, W. Zhang, H-S. Zhang, D-F. Yang, *Atmospheric Environment*, **2007**, 41, 6853.
[12] I. Aouadi, J. M. Tatibouet, and L. Bergaoui, *Plasma Chem. Plasma Process.*, **2016**, 36, 1485.
[13] A. Maciuca, C. Batiot-Dupeyrat, and J. M. Tatibouët,

Appl. Catal. B Environ., **2012**, 125, 432.
[14] V. R A. Drits, E. Silvester, A. I. Gorshkov, A. Manceau, *American Mineralogist*, **1997**, 82 946.
[15] Q. Feng, K. Yanagisawa, and N. Yamasaki, *J. Porous Mater.*, **1998**, 153.
[16] Q. Feng, Chem. Mater., **1995**, 7, 1722.
[17] Z. Sun, H. Chen, D. Shu, C. He, S. Tang, and J. Zhang, *J. Power Sources*, **2012**, 203, 233.
[18] C. Julien, M. Massot, R. Baddour-Hadjean, S. Franger, S. Bach, and J. P. Pereira-Ramos, *Solid State Ionics*, **2003**, 159, 345.
[19] C. Julien, M. Massot, and C. Poinsignon, *Spectrochim. Acta Part A Mol. Biomol. Spectrosc.*, **2004**, 689.
[20] A. Ogata, S. Komaba, R. Baddour-Hadjean, J. P. Pereira-Ramos, and N. Kumagai, *Electrochim. Acta*, **2008**, 53, 3084.
[21] H.-S. Kim and P. C. Stair, *J. Phys. Chem. B*, **2004**, 108, 17019.
[22] C. Julien and M. Massot, *Phys. Chem. Chem. Phys.*, **2002**, 4, 4226.
[23] Q. Feng, L. Liu, and K. Yanagisawa, *J. Mater. Sci. Lett.*, **2000**, 19, 1567.
[24] W. Y. Hernández, M. A. Centeno, F. Romero-sarria, S. Ivanova, M. Montes, and J. A. Odriozola, *Catalysis Today*, **2010**, 157, 160.
[25] D. A. Links, Chem. Chem. Phys., **2011**, 13, 4463.
[26] J. Zhang, Y. Li, L. Wang, C. Zhang, and H. He, *Catal. Sci. Technol.*, **2015**, 5, 2305.
[27] Y. Li, Z. Fan, J. Shi, Z. Liu, and W. Shangguan, *Chem. Eng. J.*, **2014**, 241, 251.
[28] S. Muhammad, E. Saputra, H. Sun, J. de C. Izidoro, D.A. Fungaro, M. Ang, M. O. Tade´ and S. Wang, *RSC Advances*, **2012**, 2, 5645.
[29] J. Liqiang, Q. Yichun, W. Baiqi, and L. Shudan, Solar Energy Materials & Solar Cells, **2006**, 90, 1773.
[30] Q. Zhao, P. Wu, B. L. Li, Z. M. Lu, E. Y. Jiang, Q. Zhao, P. Wu, B. L. Li, Z. M. Lu, and E. Y. Jiang, *J. Appl. Phys.*, **2008**, 104, 2.
[31] L. Kernazhitsky, V. Shymanovska, T. Gavrilko, V. Naumov, L. Fedorenko, and V. Kshnyakin, *J. Nano-and Electron. Phys.*, **2013**, 5, 1.
[32] Y. Lei, L. D. Zhang, G. W. Meng, G. H. Li, X. Y. Zhang, C. H. Liang, W. Chen, S. X. Wang, Y. Lei, L. D. Zhang, G. W. Meng, G. H. Li, X. Y. Zhang, C. H. Liang, and W. Chen, *Appl. Phys. Lett.*, **2001**, 78, 1999.
[33] T. Boningari, P. R. Ettireddy, A. Somogyvari, Y. Liu, A. Vorontsov, C. A. Mcdonald, and P. G. Smirniotis, *J. Catal.*, **2015**, 325, 145.
[34] L. Lamaita, M. A. Peluso, J. E. Sambeth, and H. J. Thomas, *Appl. Catal. B Environ.*, **2005**, 61, 114.
[35] M. A. Peluso, J. E. Sambeth, and H. J. Thomas, *React. Kinet. Catal. Lett.*, **2003**, 80, 241.
[36] R. Xu, X. Wang, D. Wang, K. Zhou, and Y. Li, Journal of Catalysis, **2006**, 237, 426.
[37] H. Einaga, T. Ibusuki, and S. Futamura, *IEEE Trans. Ind. Appl.*, **2001**, 37, 1476.
[38] W. Li, G. V Gibbs, S. T. Oyama, and R. V April, *J. Am. Chem. Soc.*, **1998**, 120, 9041.
[39] A. Maciuca, C. Batiot-Dupeyrat, and J. Tatibouët, *Int. J. Plasma Environ. Sci. Technol.*, **2012**, 6, 135.